ARTICLES
PUBLISHED ONLINE: 22 JULY 2011 | DOI: 10.1038/NCHEM.1095
nature chemistry

Single-atom catalysis of CO oxidation using Pt_1/FeO_x

Botao Qiao[1], Aiqin Wang[1], Xiaofeng Yang[2], Lawrence F. Allard[3], Zheng Jiang[4], Yitao Cui[5], Jingyue Liu[1,6]*, Jun Li[2]* and Tao Zhang[1]*

Platinum-based heterogeneous catalysts are critical to many important commercial chemical processes, but their efficiency is extremely low on a per metal atom basis, because only the surface active-site atoms are used. Catalysts with single-atom dispersions are thus highly desirable to maximize atom efficiency, but making them is challenging. Here we report the synthesis of a single-atom catalyst that consists of only isolated single Pt atoms anchored to the surfaces of iron oxide nanocrystallites. This single-atom catalyst has extremely high atom efficiency and shows excellent stability and high activity for both CO oxidation and preferential oxidation of CO in H_2. Density functional theory calculations show that the high catalytic activity correlates with the partially vacant 5*d* orbitals of the positively charged, high-valent Pt atoms, which help to reduce both the CO adsorption energy and the activation barriers for CO oxidation.

Supported noble-metal catalysts are the most widely used in industry because of their high activity and/or selectivity for a large number of important chemical reactions. Generally, in such systems noble metals are dispersed finely on a support with a high surface area for the efficient use of catalytically active components. The size of metal particles is therefore one of the most important factors that dictate the performance of a catalyst[1–4]. Recent theoretical and experimental results demonstrated that sub-nanometre clusters have better catalytic activity and/or selectivity than nanometre-sized particles[3–7]. Low-coordination, unsaturated atoms often function as active sites[8], so downsizing the particles or clusters to single atoms is highly desirable for catalytic reactions. However, fabrication of practical and stable single-atom catalysts remains a significant challenge because, typically, single atoms are too mobile and easy to sinter under realistic reaction conditions[9,10]. Moreover, it remains unclear whether single atoms can be catalytically active or have better performance than the corresponding (sub)nanometre-sized clusters or particles[3,9,11,12].

Although mass-selected clusters (or even single atoms) soft-landed on oxide supports are used for fundamental studies[6,13,14], such an expensive and low-yield fabrication method is not suitable for practical applications. A more realistic approach is to tune conventional chemical methods to anchor single metal atoms on special sites of oxide supports. Many studies on oxide-supported metal clusters show that surface defects of the supports could serve as anchoring sites for metal clusters or even single atoms[2,15,16]. Here we report the first practical fabrication of a Pt single-atom catalyst that consists only of isolated single atoms anchored onto iron oxide (FeO_x) nanocrystallites. This Pt single-atom catalyst exhibits very high activity and stability for both CO oxidation and preferential oxidation (PROX) of CO in H_2, attributed to the partially vacant 5*d* orbitals of positively charged, high-valent Pt atoms.

Results and discussion

Preparation. The single-atom Pt_1/FeO_x catalyst (denoted as sample A, with a Pt/Fe atomic ratio of 1/1430 and a Pt loading of 0.17 weight percent (wt%)) was prepared by a co-precipitation method reported previously for supported Au and Pd catalysts[17,18], but with a finely tuned co-precipitation temperature and pH value. Specifically, to anchor Pt atoms onto the defects of the FeO_x surfaces and to isolate the Pt atoms sufficiently, we controlled the Pt loading to 0.17 wt% and used a FeO_x nanocrystallite support with a high surface area (approximately 290 $m^2\ g^{-1}$ for the as-synthesized samples). To evaluate the effect of Pt loading on the structure and performance of the final catalysts, a similar catalyst with a Pt loading of 2.5 wt% (denoted as sample B, with a Pt/Fe atomic ratio of 1/95) was also prepared, characterized and tested.

Electron microscopy. Subångström-resolution, aberration-corrected scanning transmission electron microscopy (STEM) was used to characterize the dispersion and configuration of the Pt clusters in the catalysts. Individual heavy atoms in practical catalysts can be discerned in the atomic resolution high-angle annular dark-field (HAADF) images[3,9,10,19–25]. For sample A, Fig. 1a clearly shows individual Pt atoms (marked by the white circles) uniformly dispersed on the surfaces of FeO_x nanocrystals. Examination of different regions revealed that only Pt single atoms are present in sample A; additional representative images are shown in Supplementary Fig. S1. The subångström-resolution HAADF image in Fig. 1b reveals clearly that individual Pt atoms (white circles) occupy exactly the positions of the Fe atoms. As plan-view HAADF images represent the projection of atoms along the incident beam direction, surface atoms cannot be distinguished from the subsurface atoms in the HAADF images. However, whether the Pt atoms are inside the FeO_x nanocrystallites can be determined by changing the focus of the electron beam (or 'depth sectioning')[26,27]. By analysing images obtained sequentially with varying beam focus settings, we concluded that the observed Pt atoms were not located inside the individual FeO_x nanocrystals. In addition, by examining many HAADF images of sample A, we estimated that the density of Pt single atoms was about 0.07 Pt atoms nm^{-2}, which is very close to the actual Pt

[1]State Key Laboratory of Catalysis, Dalian Institute of Chemical Physics, Chinese Academy of Sciences, Dalian 116023, China, [2]Department of Chemistry, Tsinghua University, Beijing 100084, China, [3]Materials Science and Technology Division, Oak Ridge National Laboratory, Oak Ridge, Tennessee 37831, USA, [4]Shanghai Synchrotron Radiation Facility, Shanghai Institute of Applied Physics, Chinese Academy of Sciences, Shanghai 201204, China, [5]State Key Laboratory of Molecular Reaction Dynamics, Dalian Institute of Chemical Physics, Chinese Academy of Sciences, Dalian 116023, China, [6]Center for Nanoscience, Department of Physics & Astronomy, and Department of Chemistry & Biochemistry, University of Missouri-St Louis, Missouri 63121, USA. *e-mail: taozhang@dicp.ac.cn; liuj@umsl.edu; junli@tsinghua.edu.cn

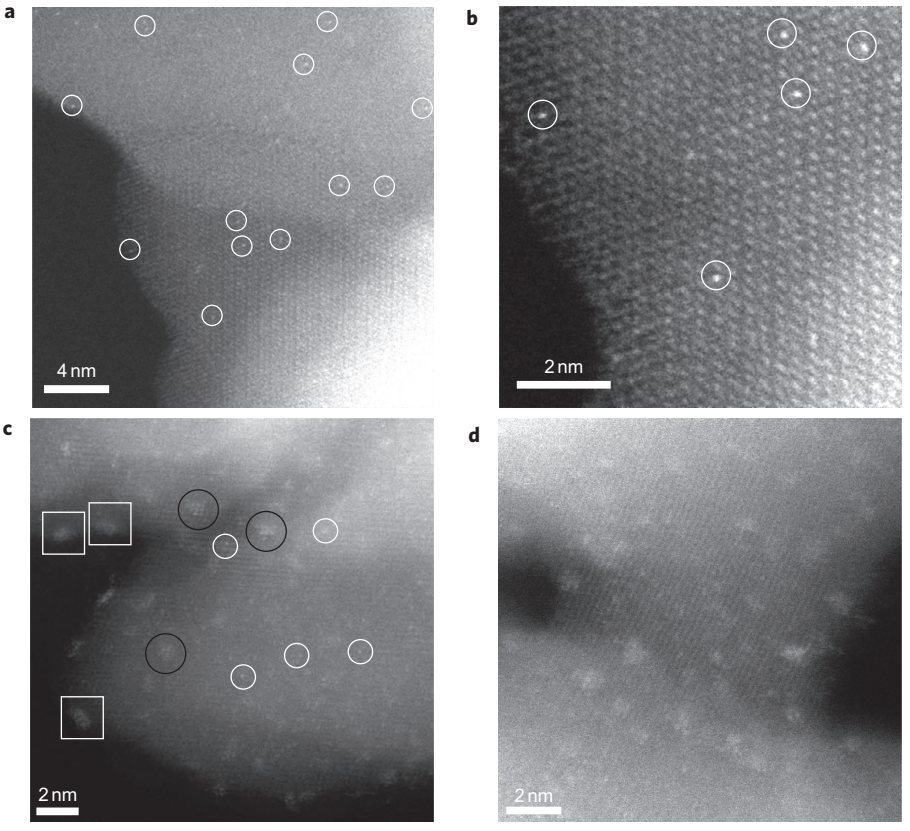

Figure 1 | HAADF-STEM images of samples A and B. a,**b**, In sample A, Pt single atoms (white circles) are seen to be uniformly dispersed on the FeO_x support (**a**) and occupy exactly the positions of the Fe atoms (**b**). Examination of different regions reveals that only Pt single atoms are present in sample A. **c**,**d**, In sample B, a mixture of single atoms (white circles), two-dimensional Pt rafts consisting of fewer than 10 Pt atoms (black circles) and three-dimensional Pt clusters of size about 1 nm or less (white squares) are observed clearly.

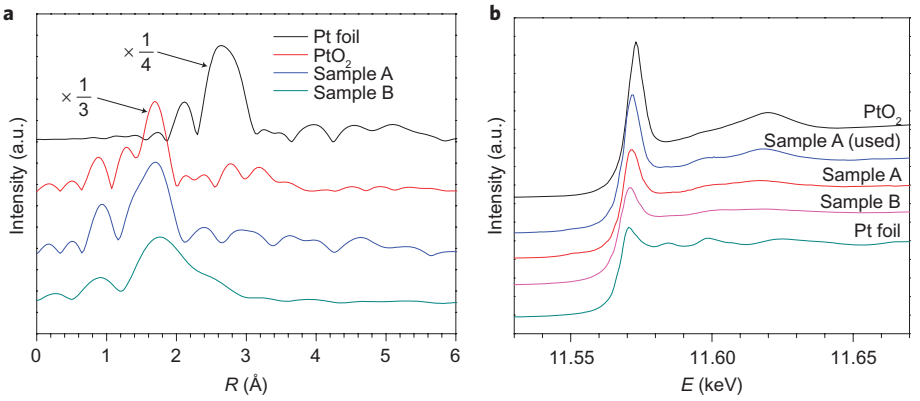

Figure 2 | X-ray absorption studies. a, The k^3-weighted Fourier transform spectra from EXAFS. $\Delta k = 2.8$–10.0 Å^{-1} was used for samples A and B, but $\Delta k = 2.8$–13.8 Å^{-1} was used for Pt foil and PtO_2. The peaks at ~1.7 Å in the first shell of samples A and B are fitted to the Pt–O contribution from the interaction between Pt and the FeO_x support, and the very weak peaks at ~2.5 Å in the second shell are fitted to the Pt–Fe coordination in sample A and the Pt–Pt coordination in sample B, respectively. **b**, The normalized XANES spectra at the Pt L_3 edge of sample A, sample B, PtO_2 and Pt foil. The data show a decreasing trend in the white-line intensities: PtO_2 > sample A (used) > sample A > sample B > Pt foil, which indicates that the Pt single atoms in sample A carry positive charges and were oxidized further during the reaction. a.u. = arbitrary units.

loading (about 0.09 Pt atoms nm^{-2}) of sample A. Therefore, all the observed individual Pt atoms are located either on the surfaces or in the near subsurfaces of the FeO_x nanocrystallites.

The Pt dispersion in sample B is quite different from that in sample A. As revealed clearly in Fig. 1c,d, sample B contained individual Pt atoms (white circles), two-dimensional Pt rafts with fewer than ten Pt atoms (black circles) and three-dimensional Pt clusters (white squares) of size ≤1 nm. On examining various regions of sample B, we did not detect any Pt nanoparticles with sizes >2 nm in diameter; Supplementary Fig. S2 shows more examples of such images. Quantitative analysis of many images suggested that the individual Pt atoms and the Pt (sub)nanometre structures in sample B account for about 27% and 73%, respectively, in terms of their frequency of observation (Supplementary Fig. S3). However, a rough estimate revealed that the single atoms represent only about 1.8 atom% of the total amount of Pt in sample B.

Table 1 | EXAFS parameters of samples A and B.

Sample	Shell	*N*	*R* (Å)	$\Delta\sigma^2 \times 10^3$ (Å^2)	ΔE_0 (eV)
Pt foil	Pt–Pt	12.0	2.81		
PtO_2	Pt–O	6.0	2.07		
	Pt–Pt	6.0	3.01		
Sample B	Pt–O	2.0	1.98	1.76	2.3
	Pt–Pt	3.8	2.53	7.22	−10.0
Sample A (Model I*)	Pt–O	1.9	2.02	4.19	9.8
	Pt–Fe	0.9	2.88	1.73	−10.0
Sample A (used)	Pt–O	3.6	2.01	4.93	8.5
	Pt–Fe	1.4	2.56	13.0	10.0

N, coordination number; *R*, distance between absorber and backscatter atoms; $\Delta\sigma^2$, change in the Debye–Waller factor value relative to the Debye–Waller factor of the reference compound; ΔE_0, inner potential correction to account for the difference in the inner potential between the sample and the reference compound. Error bounds (accuracies) that characterize the structural parameters obtained by EXAFS spectroscopy were estimated as *N*, ±20%; *R*, ±1%; $\Delta\sigma^2$, ±20%; ΔE_0, ±20%. Pt foil parameter from data_41525-ICSD; PtO_2 parameter from data_24923-ICSD; *r* space fit, $\Delta k = 2.8$–10.0 Å^{-1}, $\Delta r = 1.0$–3.2 Å, 13 statistically justified free parameters; S_0^2 fitting from PtO_2 foil defined as 0.95. *For details see the Supplementary Information.

X-ray absorption fine structure studies. Consistent with the HAADF image analyses, X-ray diffraction patterns of samples A and B (Supplementary Fig. S4) did not show any Pt-containing crystal phases, primarily because of the insensitivity of X-ray diffraction to small clusters. To verify further that sample A contained only atomically dispersed individual Pt atoms throughout the whole catalyst, extended X-ray absorption fine structure (EXAFS) spectra were measured on freshly reduced catalysts. The EXAFS spectra of both sample A and sample B at the Pt L_3 edge are characterized by the absence of oscillations at a high *k* region of $k > 8$ Å^{-1} (Supplementary Fig. S5) that indicates the dominance of low *Z* backscatters, which should be oxygen in our system. Correspondingly, in the Fourier transforms (*r* space, Fig. 2a) of the EXAFS data, there is one prominent peak at ~1.7 Å from the Pt–O contribution and a very weak peak at ~2.5 Å from either the Pt–Pt or the Pt–Fe contributions. Owing to the high disordering in the higher shells, only the two main peaks in the *r* range of 1.0–3.2 Å were considered in the EXAFS curve-fitting (fitting parameters are given in Table 1). There were Pt–O contributions at a distance of 2.02 Å for sample A and of 1.98 Å for sample B; their coordination number was around 2.0. The samples were pre-reduced before the EXAFS measurements, so PtO_x phases should not be in both samples. As a result, the Pt–O coordination originated most probably from the interaction between Pt and the FeO_x support. The observation that the Pt–O bonding distance is close to that in PtO_2 suggests the strong metal–support interaction.

For sample B, there was a Pt–Pt contribution at a distance of 2.53 Å with an average coordination number of 3.8. Both the coordination number and the Pt–Pt bonding distance in sample B are much lower than those in bulk platinum (coordination number of 12 at a distance of 2.78 Å) (ref. 28). The significantly shorter Pt–Pt bond distance in small Pt clusters was predicted by theoretical studies[29]. Our subångström-resolution HAADF images of sample B also show that most of the clusters are two-dimensional rafts and that the Pt–Pt distances in these raft-like subnanometre clusters range from 2.1 to 2.5 Å, in good agreement with the EXAFS results discussed above. From these data, we conclude that sample B contains very small Pt_x clusters.

In contrast to sample B, the second shell in sample A does not fit with Pt–Pt bonding. Comparison of three different models (Supplementary Table S1) shows that the best fit for the second shell of sample A is with a contribution of Pt–Fe at a distance of 2.88 Å, with an average coordination number of 0.9. As the nearest neighbours of Pt are O atoms, the Pt–Fe coordination originates from the next-nearest neighbour Fe bridged by the nearest oxygen atom. The EXAFS data do not reveal any Pt–Pt contribution in sample A, in agreement with the HAADF result that sample A contains only single Pt atoms.

Figure 2b shows the normalized X-ray absorption near-edge structure (XANES) spectra of samples A and B, and the reference spectra of Pt foil and PtO_2. The white line intensities in the spectra reflects the oxidation state of Pt in different samples[30], so the white-line intensity in sample A, which is between the intensities of Pt foil and PtO_2, suggests that the Pt single atoms in sample A carry positive charges. In contrast, the white-line intensity of sample B is clearly lower than that of sample A, and is similar to that of the Pt foil, which indicates the dominance of Pt^0 clusters in sample B.

Fourier transform infrared studies of CO adsorption. We investigated further the CO adsorption behaviour of the catalysts using Fourier-transform infrared (FTIR) spectroscoy to provide additional information about the dispersion and oxidation state of Pt.

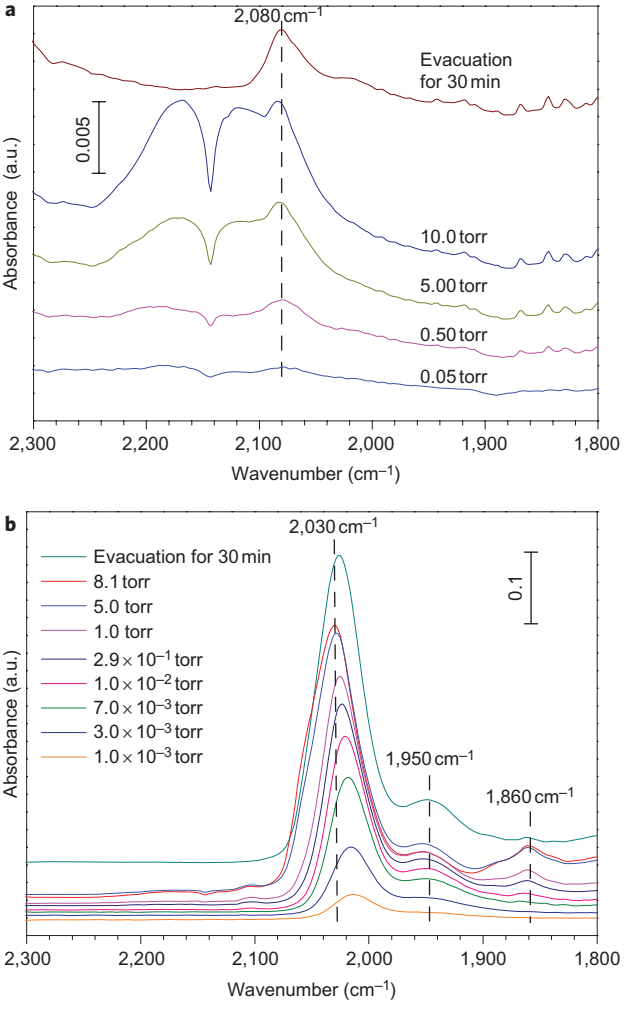

Figure 3 | *In situ* FTIR spectra of CO adsorption for samples A and B. a, For sample A, the band at 2,080 cm^{-1} is ascribed to CO, which is linearly adsorbed on $Pt^{\delta+}$. The independence of frequency with CO pressure suggests a lack of interaction between the adsorbed CO molecules, and confirms that the single Pt atoms in sample A are well isolated. **b**, For sample B, the bands at 2,030 cm^{-1}, 1,860 cm^{-1} and 1,950 cm^{-1} are, respectively, ascribed to the linearly bonded CO on Pt^0 sites, bridge-bonded CO on two Pt atoms and CO adsorbed on the interface between Pt clusters and the support. That bridge-bonded CO was detected and the frequency was blue shifted with CO pressure suggests the presence of Pt clusters in sample B.

Table 2 | Comparison of reaction rates and TOFs.

	Metal loadings (wt%)	Reaction type	Temperature (°C)	Specific rate × 10^2 (mol_{CO} h^{-1} g_{metal}^{-1})	TOF × 10^2 (s^{-1})†
Sample A	0.17	CO oxidation	27	43.5	13.6
Sample B	2.5	CO oxidation	27	17.7	8.01
Au/Fe_2O_3*	4.4	CO oxidation	27	21.7	4.76
Sample A	0.17	PROX	27	67.6	21.2
Sample B	2.5	PROX	27	20.3	9.15
Au/Fe_2O_3*	4.4	PROX	27	39.3	8.60
Sample A	0.17	PROX	80	99.2	31.1
Sample B	2.5	PROX	80	35.8	16.2
Au/Fe_2O_3*	4.4	PROX	80	80.3	17.6

*Provided by World Gold Council. †TOFs were calculated based on the metal dispersion. For samples A and B, the metal dispersion was measured by CO chemisorption conducted on a BT2.15 heat-flux calorimeter and on an Auto Chem II 2920, respectively; for Au/Fe_2O_3, the dispersion was estimated by the metal particle size according to $D = 1/d_{Au}$.

Figure 3 shows that, for sample B, the adsorption of CO produces a strong vibration band at 2,030 cm^{-1} and two other weak bands at 1,860 cm^{-1} and 1,950 cm^{-1}, respectively. The main band at 2,030 cm^{-1} can be ascribed to linearly bonded CO on Pt^0 sites, and the bands at 1,860 cm^{-1} and 1,950 cm^{-1} are caused by bridged adsorption of CO on two Pt atoms, as well as CO adsorbed on the interface between Pt clusters and the support[31]. The formation of bridge-bonded CO indicates the existence of dimer or Pt clusters, consistent with the STEM and EXAFS results that Pt clusters coexist with individual Pt atoms in sample B. In comparison to other supported Pt catalysts[32,33] (for example, Pt/SiO_2 and Pt/Al_2O_3), the terminal absorption band of CO on Pt^0 of sample B had a large red shift, consistent with the data obtained from the very small size of Pt clusters on the FeO_x support[33,34]. With an increase of CO pressure, the absorption band was blue shifted because of the coupling of adsorbed CO molecules[35]. After evacuation for 30 minutes, the intensity of the terminal band at 2,030 cm^{-1} remained almost unchanged, which indicates that the adsorption of CO on Pt^0 is irreversible.

To verify the above assignment of the band at 2,030 cm^{-1}, sample B was exposed further to oxygen following CO adsorption and evacuation. The result (Supplementary Fig. S6) shows that, with an increase of the O_2 pressure, the CO adsorption band at 2,030 cm^{-1} became weak as a new band at about 2,070 cm^{-1} evolved gradually; this suggests that Pt^0 was oxidized gradually by O_2. Thus, the band at 2,030 cm^{-1} was, indeed, caused by the linearly adsorbed CO on Pt^0 and the new band at 2,070 cm^{-1} can be assigned to CO adsorbed on $Pt^{\delta+}$ (refs 36,37).

For CO adsorption on sample A, only a weak band appeared at 2,080 cm^{-1}, which can be ascribed to CO adsorbed on $Pt^{\delta+}$. Unlike that for sample B, the band position of CO adsorbed on sample A was almost unchanged with increasing CO pressure, which suggests a lack of interaction between adsorbed CO molecules on Pt because of the isolation of single Pt atoms. Moreover, the adsorption of CO on single $Pt^{\delta+}$ atoms was rather weak and partially reversible, as indicated by the significant decrease of the peak intensity on evacuation. A more detailed investigation of CO adsorption on sample A revealed that the introduction of either H_2 or O_2 did not result in noticeable changes of the CO adsorption band (Supplementary Fig. S7), which indicates that the anchored single $Pt^{\delta+}$ atoms are stable and are not reduced in the presence of H_2 at room temperature. The systematic FTIR spectroscopy study further confirmed that sample A contained only positively charged Pt single atoms and that sample B contained both single atoms and Pt clusters.

In summary, all the characterization data discussed above provide strong evidence that sample A was composed of only isolated, positively charged single Pt atoms. The strong electrostatic and covalent interactions between the positively charged single Pt atoms and the FeO_x support helped to stabilize the single Pt atoms on the FeO_x support. As we show below, these FeO_x-stabilized single Pt atoms exhibited remarkable catalytic performance for CO oxidation and PROX reactions.

Catalytic performance. We chose CO oxidation and PROX as probe reactions to investigate the catalytic performance of FeO_x-supported single Pt atoms, as such reactions are critical in cleaning air[38] and in fuel-cell applications[39]. Table 2 lists the reaction rates and turnover frequencies (TOFs) of the two samples for CO oxidation and PROX reactions. As a reference, also the standard Au/Fe_2O_3 catalyst (provided by the World Gold Council), well-known for its high activity for CO oxidation[40], was tested under the same reaction conditions. For CO oxidation, sample A gave a specific reaction rate of 0.435 mol_{CO} h^{-1} g_{Pt}^{-1} at the reaction temperature of 27 °C, which is double that of Au/Fe_2O_3 and almost triple that of sample B. The TOFs, calculated based on the dispersion of metals on the catalysts, also revealed that sample A was ~2–3 times more active than both sample B and Au/Fe_2O_3. For the PROX reaction, all three catalysts were more active than for CO oxidation, and sample A was again ~2–3 times as active as the other two samples. This result is surprising given that the commercial Pt/Al_2O_3 catalyst is at least ~1–2 orders of magnitude less active than the standard gold nanocatalysts for low-temperature CO oxidation and PROX reactions[41]. In fact, our single-atom Pt catalyst was the most active for CO oxidation and PROX reactions among a number of supported Pt catalysts (Supplementary Table S2). The high activity of sample A must have originated from the intrinsic nature of single Pt atoms dispersed onto FeO_x surfaces, as our tests showed that the FeO_x support itself was essentially inactive for the PROX reaction at 80 °C.

Elemental analyses showed that, in addition to surface hydroxyl groups (Supplementary Fig. S8), some impurities (mainly Na^+) were present on the surface of the Pt_1/FeO_x catalyst; however, they had little effect on the catalytic activity (Supplementary Fig. S9). The single-atom Pt catalyst was stable during the PROX reaction. As shown in Supplementary Fig. S10, at a space velocity of 2.1 × 10^6 ml g_{Pt}^{-1} h^{-1}, both the CO conversion and the CO_2 selectivity over sample A remained at constant values over a 1,000 minute run at 80 °C (the typical working temperature for polymer electrolyte membrane fuel cells) without any decay, which suggests that sintering of single Pt atoms did not occur during the catalytic reactions. To evaluate the deactivation trend of sample A, we increased the space velocity by about five times to 1.1 × 10^7 ml g_{Pt}^{-1} h^{-1} and found that the CO conversion began to decrease gradually only after a 300 minute run. Concurrently, the selectivity of CO_2 began to increase (Supplementary Fig. S10), which suggests that the catalyst deactivation took place during the accelerated deactivation test and this deactivation was more prominent for the oxidation of H_2. When the catalyst bed was purged with He for 30 minutes at 200 °C, however, the deactivated catalyst regenerated completely. This

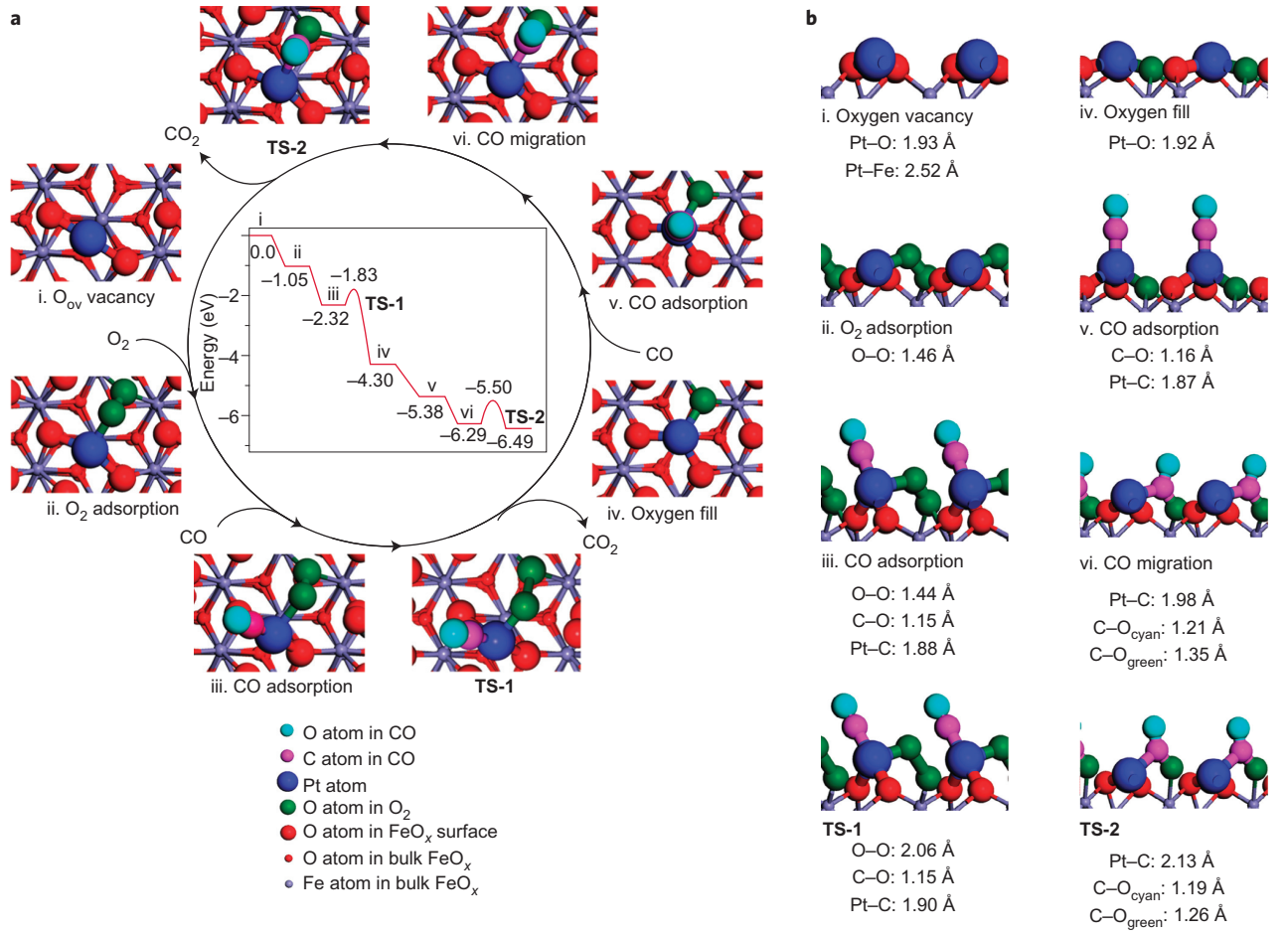

Figure 4 | The proposed reaction pathways for CO oxidation on the Pt_1/FeO_x catalyst (sample A). a,**b**, Top view (**a**) and side view (**b**). After pre-treatment by H_2, the stoichiometric haematite surfaces near the Pt atoms were reduced partially to form an O_{vac} (step i) that can adsorb the O_2 reactants (step ii) as CO is adsorbed on the single Pt atoms (step iii). Through an activation barrier of 0.49 eV (**TS-1**), the first CO_2 molecule is released and the surface oxygen vacancy is healed by the remaining O_{ad} atom of the O_2 reactant (step iv). When the second CO molecule is adsorbed at the Pt atom (step v), it migrates to a neighbouring oxygen atom (step vi) to form a transition state with a barrier of 0.79 eV (**TS-2**), which leads to a new CO oxidation. By releasing the second CO_2, the Pt-embedded stoichiometric surface is reduced again to form a new O_{vac} (step i). The inset in the cycle (**a**) shows the calculated energy profile, with the partially reduced sample A system as the reference for the energies (in eV). After one catalytic cycle, the catalyst is recovered and releases two CO_2 molecules.

result indicates that the deactivation of sample A during the accelerated deactivation test was not caused by the sintering of Pt atoms, but most probably by accumulation of carbonate species on the catalyst surface[31,42]. Further studies revealed that the Pt_1/FeO_x catalyst was stable even after two cycles of oxidation–reduction treatments (Supplementary Fig. S11).

The STEM images of the used sample A shown in Supplementary Fig. S12 reveal that the used catalyst still consists primarily of isolated single Pt atoms. The STEM images of the used catalyst provides direct evidence that the working Pt_1/FeO_x catalyst was stable and that there was no observable agglomeration of the individual Pt atoms during the catalytic reactions. To study further the changes of the oxidation state of the Pt_1/FeO_x catalyst during the reaction, we conducted *in situ* diffuse reflectance infrared Fourier transform spectroscopy (Supplementary Fig. S13) experiments under the PROX reaction conditions. The absorption band of CO adsorbed on sample A had a small blue shift with the time on stream, which suggested that the Pt single atoms were oxidized slightly during the PROX reaction. The XANES and EXAFS data of the used catalyst also confirmed that the oxidation state of the Pt single atoms was increased, as shown by the increased white-line intensity and the Pt–O coordination number (Fig. 2 and Table 1). There was still no evidence of the formation of Pt–Pt bonding in the used catalyst (Table 1), which corroborates the STEM results discussed above.

Density functional theory studies. To elucidate the nature of the binding of Pt single atoms to the FeO_x support and the exceptionally high catalytic activity of single Pt atoms, we carried out extensive theoretical investigations using relativistic density functional theory (DFT). α-Fe_2O_3 has a hexagonal corundum structure with antiferromagnetism. The (001) surface is one of the predominant growth surfaces, and single Fe-terminated, double Fe-terminated and O_3-terminated surfaces can form when different surface atoms are exposed[43–45]. However, previous experimental and theoretical results revealed that the Fe-terminated Fe_2O_3(001) surface is the inherently most stable surface[43,46–48], which indicates that most probably the Fe-terminated Fe_2O_3(001) surface was exposed in the supported catalysts. We compared the stabilities of Pt located at different sites on the three differently terminated Fe_2O_3(001) surfaces. As shown in Supplementary Fig. S14 and Supplementary Table S3, our DFT calculations indicate that the most probable sites for single Pt atoms on the various possible Fe_2O_3 surfaces are the three-fold hollow sites on the O_3-terminated surface, where each Pt atom is coordinated by three surface oxygen atoms, with the

third-layer Fe atoms below the Pt atoms (Supplementary Fig. S15). This location of Pt can be viewed as the surface Fe atoms on the surface terminated by single Fe atoms being replaced by single Pt atoms, consistent with the results from the HAADF images that Pt atoms occupy exactly the positions of the Fe atoms. The DFT calculations show that the formation of an oxygen vacancy (O_{vac}), defined as the energy needed to form one oxygen vacancy on the surface and half an oxygen molecule in the gas phase, is much lower on the Pt-terminated surface (~1.06 eV) than that on the most-stable Fe-terminated surface of the Fe_2O_3 support (~2.99 eV), in agreement with the temperature-programmed reduction result (Supplementary Fig. S16). This result indicates that the presence of individual Pt atoms can improve greatly the reducibility of the Fe_2O_3 support. Moreover, the Bader charge analysis (Supplementary Table S4) shows that the Pt atoms carry considerable positive charges (+0.45 |e|), which indicates significant electron transfer from Pt atoms to the FeO_x support. The stretching vibration frequency of CO adsorbed on Pt single atoms was calculated as 2,062 cm^{-1}, a blue shift of 44 cm^{-1} relative to the frequency of CO adsorbed on a free Pt_{10} cluster. This frequency shift is in excellent agreement with our observed infrared spectra. The calculated adsorption energy for CO is much lower (1.96 eV) on the single Pt atoms embedded in the FeO_x support than on the free Pt_{10} clusters (3.05 eV). All these results suggest that the Pt single atoms embedded into the Fe_2O_3 surface had a high oxidation state because of coordination by the three surface O atoms, significantly different from that of Pt atoms in clusters or metal surfaces. Bonding analysis on model systems showed that the back-donating interaction between CO and Pt was much less for Pt_1/FeO_x than for Pt_x clusters, and so the more-vacant *d* orbitals of the individual Pt atoms in the Pt_1/FeO_x catalyst play a vital role in the remarkable catalytic activity of this catalyst (Supplementary Fig. S17). These explain the low CO-adsorption energy, which reduces the effect of CO poisoning and facilitates the adsorption of oxygen, and thus enhances the activity of CO oxidation on the Pt single-atom sites.

The catalytic cycle of CO oxidation over the single atom Pt catalyst from the DFT calculations is summarized in Fig. 4. After pre-reduction by H_2, the stoichiometric haematite surfaces near the Pt atoms are reduced partially to form an oxygen vacancy (step i), which can adsorb the O_2 reactants. In this model, an O_{vac} near the Pt atoms is used to model the reduced FeO_x surfaces. In this case, the oxygen-coordination number of Pt changes from three to two, consistent with the EXAFS-fitting result on freshly reduced Pt_1/FeO_x catalyst. The calculated adsorption energy of O_2 (1.05 eV) and the O–O bond length (1.46 Å) suggest that the adsorbed oxygen ($O_{2,ad}$) is well activated over Pt single atoms (step ii). The adsorption of CO on the single Pt atoms has a binding energy of 1.27 eV (step iii), which is much lower than that we calculated for a Pt_x cluster. The calculated activation barrier for reaction of $CO_{ad} + O\text{–}O_{ad} \rightarrow CO_2 + O_{ad}$ (**TS-1**) is 0.49 eV. After the release of the CO_2 molecule the surface oxygen vacancy is healed by the remaining O_{ad} atom of the O_2 reactant, which restores the Pt-substituted stoichiometric haematite surfaces (step iv). When the second CO molecule is adsorbed at Pt (step v), a new reaction of $CO_{ad} + O_{ad} \rightarrow CO_2 + O_{vac}$ occurs (step vi and **TS-2**). The calculated barrier of this reaction is 0.79 eV. After releasing the second CO_2, the Pt-embedded stoichiometric surface is reduced again to form a new oxygen vacancy (step i). This multi-step procedure thus finishes the catalytic cycle. The two CO oxidation reactions of $CO_{ad} + O\text{–}O_{ad}$ and $CO_{ad} + O_{ad}$ both follow Langmuir–Hinshelwood mechanisms. The activation barriers on the single Pt atoms are remarkably lower than that (~1 eV) of CO oxidation on Pt(111) (ref. 49). All the elementary steps in the catalytic cycle are exothermic and the barriers are low enough for CO oxidation at low temperatures. Thus the Pt_1/FeO_x catalyst has well-balanced thermodynamics and kinetics for CO oxidation and the PROX reactions.

Conclusions

In summary, we synthesized and characterized a novel catalyst that consists of only single Pt atoms uniformly dispersed on a FeO_x support of high surface area. This catalyst showed extremely high activity for both CO oxidation and PROX reactions. The chemical reactivity of our positively charged single Pt atoms is quite different from that of single Au atoms or cations on the same support; the commercial Au/FeO_x catalyst contains polydispersed nanostructures from single atoms to clusters, with single Au atoms reported to be inactive for CO oxidation[3,27,50]. The more vacant *d* orbitals of the single Pt atoms, because of the electron transfer from Pt atoms to the FeO_x surface, are responsible both for the strong binding and stabilization of single Pt atoms and for providing positively charged Pt atoms, which ultimately account for the excellent catalytic activity of the Pt_1/FeO_x catalyst. Although we used CO oxidation to demonstrate the high activity of the Pt_1/FeO_x catalyst, the observed behaviour of single Pt atoms is, nonetheless, not limited to CO oxidation. Moreover, the stabilization of single atoms on practical oxide supports via the charge-transfer mechanism is not limited to the Pt_1/FeO_x system, but can be extended further and made applicable to other precious-metal systems. The discovery of this single-atom Pt catalyst not only proves the concept of single-atom heterogeneous catalysis, but also has a great potential to reduce the high cost of commercial noble-metal catalysts in industry.

Methods

Sample preparation. Both sample A and sample B were prepared by co-precipitation of an aqueous solution of chloroplatinic acid ($H_2PtCl_6{\cdot}6H_2O$, 7.59×10^{-2} mol l^{-1}) and ferric nitrate ($Fe(NO_3)_3{\cdot}9H_2O$, 1 mol l^{-1}) with sodium carbonate (Na_2CO_3, 1 mol l^{-1}) at 50 °C, with the pH value of the resulting solution controlled at about 8. The recovered solid was dried at 60 °C for five hours and calcined at 400 °C for five hours. Prior to being characterized and tested, the samples were reduced in 10% H_2/He at 200 °C for 0.5 hours. The actual Pt loadings in the two samples, determined by inductively coupled plasma spectroscopy on an IRIS Intrepid II XSP instrument (Thermo Electron Corporation), were 0.17 wt% for sample A and 2.50 wt% for sample B.

Sample characterization. Subångström resolution HAADF STEM images were obtained on a JEOL JEM 2200FS STEM/TEM, equipped with a CEOS (Heidelburg, Ger) probe corrector, and a nominal image resolution of 0.07 nm, and on a JEOL JEM-ARM200F STEM/TEM, also equipped with a CEOS probe corrector, with a guaranteed resolution of 0.08 nm. Before microscopy examination, the samples were dry dispersed onto a copper grid coated with a thin holey carbon film.

Pt L_3-edge absorption spectra (EXAFS) were performed on two beamlines. One was the BL14W1 beamline at the Shanghai Synchrotron Radiation Facility (SSRF), Shanghai Institute of Applied Physics (SINAP), China, operated at 3.5 GeV with injection currents of 140–210 mA. The other was the 1W1B beamline of the Beijing Synchrotron Radiation Facility (BSRF) operated at ~200 mA and ~2.2 GeV. On both beamlines, a Si(111) double-crystal monochromator was used to reduce the harmonic component of the monochrome beam. Pt foil and PtO_2 were used as reference samples and measured in the transmission mode, and both sample A and sample B were measured in fluorescence mode. Before measurement, the powder sample was pre-reduced at 200 °C for 30 minutes (the same pre-treatment condition as that used for the activity test) in a specially designed reactor equipped with shut-off valves at both ends. Prior to disconnection with the flowing hydrogen, the valves on the reactor were closed so that the freshly reduced sample was not exposed to air. After that, the reactor was transferred into an argon-filled glove box and the sample taken out and pressed into a self-supporting disk. The disk was then sealed with Kapton membrane and subjected to EXAFS measurement. For comparison, sample A after the PROX reaction (denoted as used catalyst) was also measured for EXAFS, but without sealing treatment. To obtain a much better signal-to-noise ratio, filters were used to reduce the fluorescence of Fe in addition to extending the integral time. We used IFEFFIT software to calibrate the energy scale, to correct the background signal and to normalize the intensity. A similar approach was used to analyse the EXAFS data at the Pt L_3 edge. Reliable parameters for the high *Z* (Pt, Fe) and low *Z* (O) contributions were determined by multiple-shell fitting in *r* space with application of k^3 and k^1 weightings in the Fourier transformations.

FTIR spectra for CO adsorption on the two samples were collected at 20 °C with a Bruker Equinox 55 spectrometer equipped with a mercury cadmium telluride detector at a resolution of 4 cm^{-1} using 60 scans for sample B and 300 scans for sample A. Before CO adsorption, the samples were reduced *in situ* at 200 °C with

10% H_2/He for 0.5 hours and then evacuated at 210 °C for 0.5 hours. The probing gases CO, H_2 and O_2 were purified with liquid nitrogen.

Catalytic testing. The catalytic performance of samples A and B for CO oxidation and PROX was evaluated in a fixed-bed reactor. Prior to the tests, the samples were pelletized and sieved to 40 and 60 mesh for use. Approximately 80 mg of the sample was loaded into a U-shaped quartz reactor, and then was reduced *in situ* with 10 vol% H_2/He at 200 °C for 0.5 hours. After cooling to 80 °C, the feed gas containing 1 vol% CO, 1 vol% O_2 and balance He was allowed to pass through the reactor at a flow rate of 25 ml min^{-1} (corresponding to a space velocity of 18,750 ml h^{-1} g_{cat}^{-1}). The effluent gas compositions were analysed on-line by a gas chromatograph (HP 6890) equipped with a TDX-01 column and a thermal conductivity detector. Also, the PROX reaction was employed as the probe reaction, for which the feed gas was composed of 40 vol% H_2, 1 vol% CO, 1 vol% O_2 and balance He. A 4.4 wt% Au/Fe_2O_3 sample from the World Gold Council was evaluated for comparison. For both CO oxidation and PROX reactions, the CO and O_2 conversions were calculated based on the difference between inlet and outlet concentrations. The selectivity (denoted as S) towards CO_2 in the PROX reaction was calculated as:

$$S = \frac{0.5 \times C_{CO}}{C_{O_2}} \times 100 \quad (1)$$

where C_{CO} and C_{O_2} represent the conversion of CO and O_2, respectively.

For measurements of specific reaction rates, both CO oxidation and PROX reactions were conducted in a differential mode in which the CO conversions were controlled below 15%. Towards this goal, ~10–20 mg of the sample with a pellet size of 200 mesh was diluted with 150 mg SiC (pellet size was also around 200 mesh). For each run at a specified reaction temperature, the CO conversions at 20 minutes, 40 minutes and 60 minutes were averaged and used for calculations of the specific rate. The TOF was then calculated based on the specific rate and the dispersion of Pt; the latter was obtained by CO chemisorption. An exception was for 4.4 wt% Au/Fe_2O_3, of which the dispersion of Au could not be obtained by CO chemisorption and therefore was estimated roughly according to the relationship between the dispersion (D) and particle diameter (d), $D = 1/d_{Au}$.

The theoretical methods and computational details, as well as the bonding analysis, are described in the Supplementary Information.

Received 7 April 2011; accepted 15 June 2011; published online 22 July 2011

References

1. Haruta, M. Size- and support-dependency in the catalysis of gold. *Catal. Today* **36,** 153–166 (1997).
2. Chen, M. & Goodman, D. W. The structure of catalytically active gold on titania. *Science* **306,** 252–255 (2004).
3. Herzing, A. A., Kiely, C. J., Carley, A. F., Landon, P. & Hutchings, G. J. Identification of active gold nanoclusters on iron oxide supports for CO oxidation. *Science* **321,** 1331–1335 (2008).
4. Turner, M. *et al.* Selective oxidation with dioxygen by gold nanoparticle catalysts derived from 55-atom clusters. *Nature* **454,** 981–983 (2008).
5. Vajda, S. *et al.* Subnanometre platinum clusters as highly active and selective catalysts for the oxidative dehydrogenation of propane. *Nature Mater.* **8,** 213–216 (2009).
6. Judai, K., Abbet, S., Worz, A. S., Heiz, U. & Henry, C. R. Low-temperature cluster catalysis. *J. Am. Chem. Soc.* **126,** 2732–2737 (2004).
7. Lei, Y. *et al.* Increased silver activity for direct propylene epoxidation via subnanometer size effects. *Science* **328,** 224–228 (2010).
8. Remediakis, I. N., Lopez, N. & Nørskov, J. K. CO oxidation on rutile-supported Au nanoparticles. *Angew. Chem. Int. Ed.* **44,** 1824–1826 (2005).
9. Uzun, A., Ortalan, V., Browning, N. D. & Gates, B. C. A site-isolated mononuclear iridium complex catalyst supported on MgO: characterization by spectroscopy and aberration-corrected scanning transmission electron microscopy. *J. Catal.* **269,** 318–328 (2010).
10. Uzun, A., Ortalan, V., Hao, Y., Browning, N. D. & Gates, B. C. Nanoclusters of gold on a high-area support: almost uniform nanoclusters imaged by scanning transmission electron microscopy. *ACS Nano* **3,** 3691–3695 (2009).
11. Kaden, W. E., Wu, T., Kunkel, W. A. & Anderson, S. L. Electronic structure controls reactivity of size-selected Pd clusters adsorbed on TiO_2 surfaces. *Science* **326,** 826–829 (2009).
12. Böhme, D. K. & Schwarz, H. Gas-phase catalysis by atomic and cluster metal ions: the ultimate single-site catalysts. *Angew. Chem. Int. Ed.* **44,** 2336–2354 (2005).
13. Lee, S. S., Fan, C. Y., Wu, T. P. & Anderson, S. L. CO oxidation on Au_n/TiO_2 catalysts produced by size-selected cluster deposition. *J. Am. Chem. Soc.* **126,** 5682–5683 (2004).
14. Yoon, B. *et al.* Charging effects on bonding and catalyzed oxidation of CO on Au_8 clusters on MgO. *Science* **307,** 403–407 (2005).
15. Matthey, D. *et al.* Enhanced bonding of gold nanoparticles on oxidized TiO_2(110). *Science* **315,** 1692–1696 (2007).
16. Kwak, J. H. *et al.* Coordinatively unsaturated Al^{3+} centers as binding sites for active catalyst phases of platinum on γ-Al_2O_3. *Science* **325,** 1670–1673 (2009).
17. Qiao, B. & Deng, Y. Highly effective ferric hydroxide supported gold catalyst for selective oxidation of CO in the presence of H_2. *Chem. Commun.* 2192–2193 (2003).
18. Qiao, B., Liu, L., Zhang, J. & Deng, Y. Preparation of highly effective ferric hydroxide supported noble metal catalysts for CO oxidations: from gold to palladium. *J. Catal.* **261,** 241–244 (2009).
19. Nellist, P. D. & Pennycook, S. J. Direct imaging of the atomic configuration of ultradispersed catalysts. *Science* **274,** 413–415 (1996).
20. Pennycook, S. J. *Z*-contrast stem for materials science. *Ultramicroscopy* **30,** 58–69 (1989).
21. Wang, S. *et al.* Dopants adsorbed as single atoms prevent degradation of catalysts. *Nature Mater.* **3,** 143–146 (2004).
22. Nellist, P. D. *et al.* Direct sub-angstrom imaging of a crystal lattice. *Science* **305,** 1741–1741 (2004).
23. Sohlberg, K., Rashkeev, S., Borisevich, A. Y., Pennycook, S. J. & Pantelides, S. T. Origin of anomalous Pt–Pt distances in the Pt/alumina catalytic system. *ChemPhysChem* **5,** 1893–1897 (2004).
24. Pennycook, S. J. *et al.* Aberration-corrected scanning transmission electron microscopy: from atomic imaging and analysis to solving energy problems. *Phil. Trans. R. Soc. A* **367,** 3709–3733 (2009).
25. Ortalan, V., Uzun, A., Gates, B. C. & Browning, N. D. Direct imaging of single metal atoms and clusters in the pores of dealuminated HY zeolite. *Nature Nanotech.* **5,** 506–510 (2010).
26. Li, Z. Y. *et al.* Three-dimensional atomic-scale structure of size-selected gold nanoclusters. *Nature* **451,** 46–48 (2008).
27. Allard, L. F. *et al.* Evolution of gold structure during thermal treatment of Au/FeO_x catalysts revealed by aberration-corrected electron microscopy. *J. Electron Microsc. (Tokyo)* **58,** 199–212 (2009).
28. Chang, J-R., Koningsberger, D. C. & Gates, B. C. Structurally simple supported platinum clusters prepared from $[Pt_{15}(CO)_{30}]^{2-}$ on magnesium oxide. *J. Am. Chem. Soc.* **114,** 6460–6466 (1992).
29. Xiao, L. & Wang, L. Structures of platinum clusters: planar or spherical? *J. Phys. Chem. A* **108,** 8605–8614 (2004).
30. Yoshida, H. *et al.* XANES study of the support effect on the state of platinum catalysts. *J. Synchrotron Radiat.* **6,** 471–473 (1999).
31. Pozdnyakova, O. *et al.* Preferential CO oxidation in hydrogen (PROX) on ceria-supported catalysts, part I: oxidation state and surface species on Pt/CeO_2 under reaction conditions. *J. Catal.* **237,** 1–16 (2006).
32. Greenler, R. G. *et al.* Stepped single-crystal surfaces as models for small catalyst particles. *Surf. Sci.* **152–153,** 338–345 (1985).
33. Brandt, R. K., Hughes, M. R., Bourget, L. P., Truszkowska, K. & Greenler, R. G. The interpretation of CO adsorbed on Pt/SiO_2 of two different particle-size distributions. *Surf. Sci.* **286,** 15–25 (1993).
34. Kappers, M. & Maas, J. Correlation between CO frequency and Pt coordination number. A DRIFT study on supported Pt catalysts. *Catal. Lett.* **10,** 365–373 (1991).
35. Hadjiivanov, K. I. & Vayssilov, G. N. Characterization of oxide surfaces and zeolites by carbon monoxide as an IR probe molecule. *Adv. Catal.* **47,** 307–511 (2002).
36. Bazin, P., Saur, O., Lavalley, J. C., Daturi, M. & Blanchard, G. FT-IR study of CO adsorption on Pt/CeO_2: characterisation and structural rearrangement of small Pt particles. *Phys. Chem. Chem. Phys.* **7,** 187–194 (2005).
37. Gruene, P., Fielicke, A., Meijer, G. & Rayner, D. M. The adsorption of CO on group 10 (Ni, Pd, Pt) transition-metal clusters. *Phys. Chem. Chem. Phys.* **10,** 6144–6149 (2008).
38. Xie, X., Li, Y., Liu, Z-Q., Haruta, M. & Shen, W. Low-temperature oxidation of CO catalysed by Co_3O_4 nanorods. *Nature* **458,** 746–749 (2009).
39. Fu, Q. *et al.* Interface-confined ferrous centers for catalytic oxidation. *Science* **328,** 1141–1144 (2010).
40. Haruta, M., Yamada, N., Kobayashi, T. & Iijima, S. Gold catalysts prepared by coprecipitation for low-temperature oxidation of hydrogen and of carbon monoxide. *J. Catal.* **115,** 301–309 (1989).
41. Haruta, M. Catalysis of gold nanoparticles deposited on metal oxides. *CATTECH* **6,** 102–115 (2002).
42. Huang, Y. Q., Wang, A. Q., Wang, X. D. & Zhang, T. Preferential oxidation of CO under excess H_2 conditions over iridium catalysts. *Int. J. Hydrogen Energy* **32,** 3880–3886 (2007).
43. Wang, X. G. *et al.* The hematite (α-Fe_2O_3) (0001) surface: evidence for domains of distinct chemistry. *Phys. Rev. Lett.* **81,** 1038–1041 (1998).
44. Yamamoto, S. *et al.* Water adsorption on α-Fe_2O_3 (0001) at near ambient conditions. *J. Phys. Chem. C* **114,** 2256–2266 (2010).
45. Jin, J. J., Ma, X. Y., Kim, C. Y., Ellis, D. E. & Bedzyk, M. J. Adsorption of V on a hematite (0001) surface and its oxidation: submonolayer coverage. *Surf. Sci.* **601,** 3082–3098 (2007).

46. Lübbe, M. & Moritz, W. A LEED analysis of the clean surfaces of α-Fe_2O_3 (0001) and α-Cr_2O_3 (0001) bulk single crystals. *J. Phys.: Condens. Matter* **21,** 134010 (2009).
47. Wasserman, E., Rustad, J. R., Felmy, A. R., Hay, B. P. & Halley, J. W. Ewald methods for polarizable surfaces with application to hydroxylation and hydrogen bonding on the (012) and (001) surfaces of α-Fe_2O_3. *Surf. Sci.* **385,** 217–239 (1997).
48. Thevuthasan, S. *et al.* Surface structure of MBE-grown α-Fe_2O_3(0001) by intermediate-energy X-ray photoelectron diffraction. *Surf. Sci.* **425,** 276–286 (1999).
49. Alavi, A., Hu, P., Deutsch, T., Silvestrelli, P. L. & Hutter, J. CO oxidation on Pt(111): an *ab initio* density functional theory study. *Phys. Rev. Lett.* **80,** 3650–3653 (1998).
50. Fu, Q., Saltsburg, H. & Flytzani-Stephanopoulos, M. Active nonmetallic Au and Pt species on ceria-based water–gas shift catalysts. *Science* **301,** 935–938 (2003).

Acknowledgements

We thank Y. Huang, S. Zhang, T. Hu, J. Zhang, Y. Xie and L. Zheng for their help in the EXAFS measurements and data analysis, and L. Li for infrared measurements and discussion. We also acknowledge E. Okunishi for assistance on operating the JEM ARM-200F TEM/STEM. Particularly, we thank Jeffrey T. Miller for his suggestions and comments on EXAFS analysis during the manuscript revision process. Financial support for this research work from the National Science Foundation of China (20325620, 20773124) and the Ministry of Science and Technology of China (NKBRSF 2007CB815200, 2011CB932400) is also acknowledged. Part of the electron microscopy work was conducted at the Oak Ridge National Laboratory's High Temperature Materials Laboratory, sponsored by the US Department of Energy, Office of Energy Efficiency and Renewable Energy, Vehicle Technologies Program. The calculations were performed at the Shanghai Supercomputing Center and the Computer Network Information Center, Chinese Academy of Sciences.

Author contributions

B. Qiao performed the catalyst preparation, characterizations and catalytic tests. X. Yang and J. Li conducted DFT calculations and wrote part of the paper (calculation). L.F. Allard and J. Liu conducted the STEM examinations and contributed to writing the STEM sections. Z. Jiang and Y. Cui performed measurements and data analyses of EXAFS. A. Wang and T. Zhang designed the study, analysed the data and co-wrote the paper. All the authors discussed the results and commented on the manuscript.

Additional information

The authors declare no competing financial interests. Supplementary information accompanies this paper at www.nature.com/naturechemistry. Reprints and permission information is available online at http://www.nature.com/reprints. Correspondence and requests for materials should be addressed to T.Z., J.J.L. and J.L.